bioRxiv preprint doi: https://doi.org/10.1101/2020.05.13.088054; this version posted May 15, 2020. The copyright holder for this preprint (which was not certified by peer review) is the author/funder. All rights reserved. No reuse allowed without permission.

Unraveling the interaction between doxorubicin and DNA origami nanostructures for customizable chemotherapeutic drug release

Heini Ijäs[1,2], Boxuan Shen[1], Amelie Heuer-Jungemann[3], Adrian Keller[4], Mauri A. Kostiainen[1,5], Tim Liedl[3], Janne A. Ihalainen[2] & Veikko Linko[1,5,*]

[1]Biohybrid Materials, Department of Bioproducts and Biosystems, Aalto University, P.O. Box 16100, 00076 Aalto, Finland

[2]Nanoscience Center, Department of Biological and Environmental Science, University of Jyväskylä, P.O. Box 35, 40014 Jyväskylä, Finland

[3]Faculty of Physics and Center for NanoScience (CeNS), Ludwig-Maximilians-University, Geschwister-Scholl-Platz 1, 80539 Munich, Germany

[4]Technical and Macromolecular Chemistry, Paderborn University, Warburger Str. 100, 33098 Paderborn, Germany

[5]HYBER Centre, Department of Applied Physics, Aalto University, P.O. Box 15100, 00076 Aalto, Finland

[*]Correspondence and requests for materials should be addressed to veikko.linko@aalto.fi

Doxorubicin (DOX) is a commonly employed drug in cancer chemotherapy, and its high DNA-binding affinity can be harnessed in preparing programmable DOX-loaded DNA nanostructures that can be further tailored for targeted delivery and therapeutics. Although DOX has been widely studied, the existing literature of promising DOX-loaded DNA nanocarriers remains limited and incoherent. A number of reports have overlooked the fundamentals of the DOX-DNA interaction, let alone the peculiarities arising from the complexity of the system as a whole. Here, based on an in-depth spectroscopic analysis, we characterize and optimize the DOX loading into different 2D and 3D scaffolded DNA origami nanostructures. In our experimental conditions, all of our DNA origami designs show rather similar DOX binding capacities, which are, however, remarkably lower than previously reported. To simulate the possible physiological degradation pathways, we examine the stability and DOX release properties of the complexes upon DNase I digestion, which reveals that they disintegrate and release DOX into the surroundings at characteristic rates related to the DNA origami superstructure and the loaded DOX content. In addition, we identify DOX self-aggregation and precipitation mechanisms and spectral changes linked to pH, magnesium, and DOX concentration that have been largely ignored in experimenting with DNA nanostructures and in spectroscopic analysis performed with routine UV-Vis and fluorescence techniques. Nevertheless, we demonstrate the possibility of customizing drug release profiles through rational DNA origami design. Therefore, we believe this work can be used as a guide to tailor the release profiles and develop better drug delivery systems based on DNA nanostructures.

DNA nanotechnology | DNA origami | drug delivery | intercalation | groove binding | drug release | stability | nucleases | enzymatic digestion

Introduction

The possibility to employ DNA molecules in engineering artificial nanostructures (1, 2) has drawn increasing attention during the past two decades (3–5). The intense development of DNA nanotechnology has yielded new methods to build user-defined nano-objects (6), such as DNA origami (7–14), for a variety of scientific and technological uses (15–18). In particular, these custom DNA nanoshapes show considerable promise in biomedicine and drug delivery (19–22). Rationally designed DNA nanovehicles can encapsulate and display selected cargoes (23–26), act as therapeutics themselves (27), serve as platforms for various targeting ligands and tailored nucleic acid sequences (28, 29), or directly host diverse DNA-binding drugs (30, 31). In the latter case, the most frequently used drug is anthracycline doxorubicin (DOX), a fluorescent DNA-intercalator, which is applied in the treatments of several cancer types and primarily in solid tumor growth suppression (32). Its mechanisms of anticancer and cardiotoxic actions are not fully understood, as it inhibits human type IIA DNA topoisomerase function either by poisoning the catalytic activity or preventing DNA-binding. However, it also affects multiple cellular processes through DNA intercalation and its ability to generate reactive oxygen species (ROS) (33). There are a number of reports, in which the properties and therapeutic potency of various DOX-loaded DNA nanostructures have been demonstrated using *in vitro* and *in vivo* models (34–45).

Typically, the presumed intercalation and release of DOX are characterized using straightforward spectroscopic indicators such as spectral changes of visible light absorption or DOX fluorescence quenching upon DNA binding interaction. However, besides intercalation, DOX may also be complexed with DNA through (pre-intercalation) minor-groove binding and stacking into aggregates depending on the DNA sequence, prevalent DOX concentration and experimental conditions such as the ionic strength of the solution (46–48). Spectroscopic features of DOX – *e.g.* the extent of fluorescence quenching – are likewise dependent on the mode of interaction. In addition, a recent study suggests that in some cases the accessibility of the intercalation binding sites in DNA nanostructures may be restricted (49). DOX molecules have two distinct protonation states within a physiologically relevant pH range (pH ∼4–9) and they are prone to self-aggregation at high concentrations (50). Therefore, spectroscopic properties of DOX are also subject to change in different media compositions. Overlooking the multiple factors, such as the binding site availability, DOX solubility, concentration, chosen loading and purification methods, ionic strength and pH of the solution may result in misleading interpretations of DOX loading capacity, release efficiency and

bioRxiv preprint doi: https://doi.org/10.1101/2020.05.13.088054; this version posted May 15, 2020. The copyright holder for this preprint (which was not certified by peer review) is the author/funder. All rights reserved. No reuse allowed without permission.

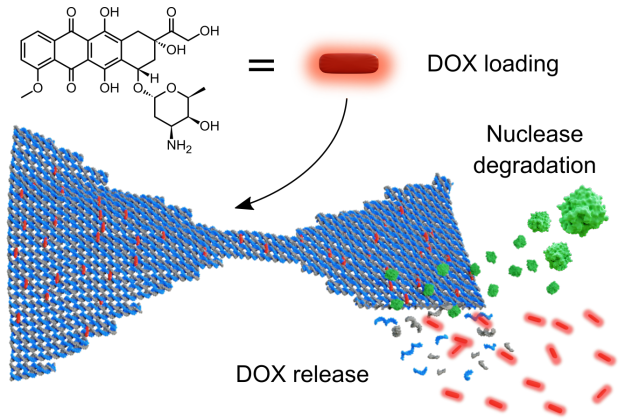

Figure 1. Schematics of the doxorubicin (DOX) loading into a DNA nanostructure and subsequent release upon enzymatic degradation. DOX molecules (red) are loaded into/onto a bowtie DNA origami (formed from blue and grey strands), and the process is optimized by monitoring the spectroscopic features of DOX, such as fluorescence quenching. The DOX is sustainedly released as DNA origami is subjected to nuclease (DNase I, green) degradation and digested into single-stranded DNA fragments. Real-time spectroscopic observation reveals that the degradation rate of DNA nanostructures and the release profiles of DOX depend on DNA origami superstructure and the applied DOX content.

thus also the therapeutic effect (22).

In this work, we systematically study the binding of DOX to five structurally distinct two- (2D) and three-dimensional (3D) scaffolded DNA origami shapes (one exemplary DNA origami design shown in Figure 1). By means of absorption, excitation and fluorescence spectroscopy techniques, we optimize the loading process and uncover the contributions of the ionic strength, pH, and DOX concentration to the measured spectra. The obtained results reveal that the DOX binding capacity of DNA origami has often been substantially overestimated, in some previously reported cases by more than two orders of magnitude.

Finally, we mimic one plausible and physiologically relevant DOX release pathway by subjecting the DOX-loaded DNA origami to deoxyribonuclease I (DNase I) digestion (see Figure 1) (51–53). Real-time monitoring of the spectroscopic changes during the digestion show that both the DNA degradation rates and the DOX release profiles depend on the DNA origami superstructure and the amount of DOX loaded. We believe that by unraveling all these fundamental and some previously undiscovered features, the engineering of new tailored DNA objects with imminent biomedical potential becomes feasible. Through identification of the loading, release and spectroscopic properties of DOX, as well as the superstructure-dependent stability factors of DNA origami in physiological conditions (54–57), it may become possible to rationally design delivery capability, control the dose and thus achieve the optimal therapeutic efficacy.

Results

Effects of buffer conditions on the spectroscopic features of DOX

To ensure that the obtained spectroscopic changes in later experiments are associated reliably with the DOX-DNA binding events and not caused by the environment, we first identified the effects of the buffer conditions on the spectroscopic properties of DOX. We performed a series of measurements on DOX in the absence of DNA in Tris-based buffers typically applied in DNA origami experiments. In particular, we screened the effect of two buffer parameters; pH and $MgCl_2$ concentration.

Buffer pH. For identifying the effects of buffer pH on the spectroscopic features of DOX, 40 mM Tris-HCl buffers were prepared at pH 6.0–9.0 and the absorption and fluorescence spectra of DOX were collected at each pH. The shape of the DOX absorption spectrum as well as its molar extinction coefficient (ϵ) depends heavily on buffer pH (Figure 2a). Between pH 6.0–8.0, the shape of the spectrum is maintained, but throughout the whole absorption spectrum, ϵ increases with decreasing pH. For instance, ϵ_{494} is *ca.* 65% higher at pH 6.0 than at pH 8.0. A higher emission intensity is also observed at lower pH values, as shown in Figure 2a inset with a 494 nm excitation.

Above pH 8.0, the shape of the absorption spectrum changes and a new absorption peak emerges at approximately 590 nm. However, exciting the molecules at this wavelength does not lead to DOX fluorescence, thus showing that at pH 8.0 and above, an increasing fraction of DOX molecules is non-fluorescent. DOX is known to have a pK_a value for the deprotonation of the amino sugar NH_3^+ group at pH 8.2 (50). The observed spectral changes and the emergence of non-fluorescent molecules take place around the same pH value, being thus likely associated with the deprotonation events. These observations are also in line with previous reports of DOX absorbance in high pH buffers (58), and the spectral changes could thus be expected to become even more pronounced at pH values above 9.0.

Near the pK_a, the sample contains a distribution of charged and neutral molecules, and in the spectroscopic means, a mixture of fluorescent and non-fluorescent DOX molecules. While the sample is thus heterogeneous, the emission spectrum remains homogeneous as the non-fluorescent molecules do not contribute to the signal (Supplementary Figure 1). As the sample heterogeneity would nevertheless complicate the interpretation of experimental results, it is beneficial to conduct experiments at pH well below the pK_a. Based on both the existing literature and the obtained spectra, an optimal pH range for further experiments was determined as 6.0–7.8, where altering the pH does not change the shape of the absorption spectrum.

Buffer $MgCl_2$ concentration at pH 7.4. DOX is known to form complexes with metal ions, such as Fe^{3+}, Cu^{2+}, Mn^{2+}, Ni^{2+}, Co^{2+}, Mg^{2+}, and Zn^{2+} (58–60). Metal ion complexation thus presents another source of DOX heterogeneity in buffers supplemented with divalent cations. When the $MgCl_2$ concentration in the buffer increases, both the absorption and fluorescence properties of DOX change indicating complexation of DOX with Mg^{2+} ions (Figure 2b). In the presence of 100 mM $MgCl_2$, three distinct peaks at 500 nm, 534 nm, and 576 nm are observed in the absorption spectrum. The 576 nm peak emerges only in the presence of $MgCl_2$, and excitation

bioRxiv preprint doi: https://doi.org/10.1101/2020.05.13.088054; this version posted May 15, 2020. The copyright holder for this preprint (which was not certified by peer review) is the author/funder. All rights reserved. No reuse allowed without permission.

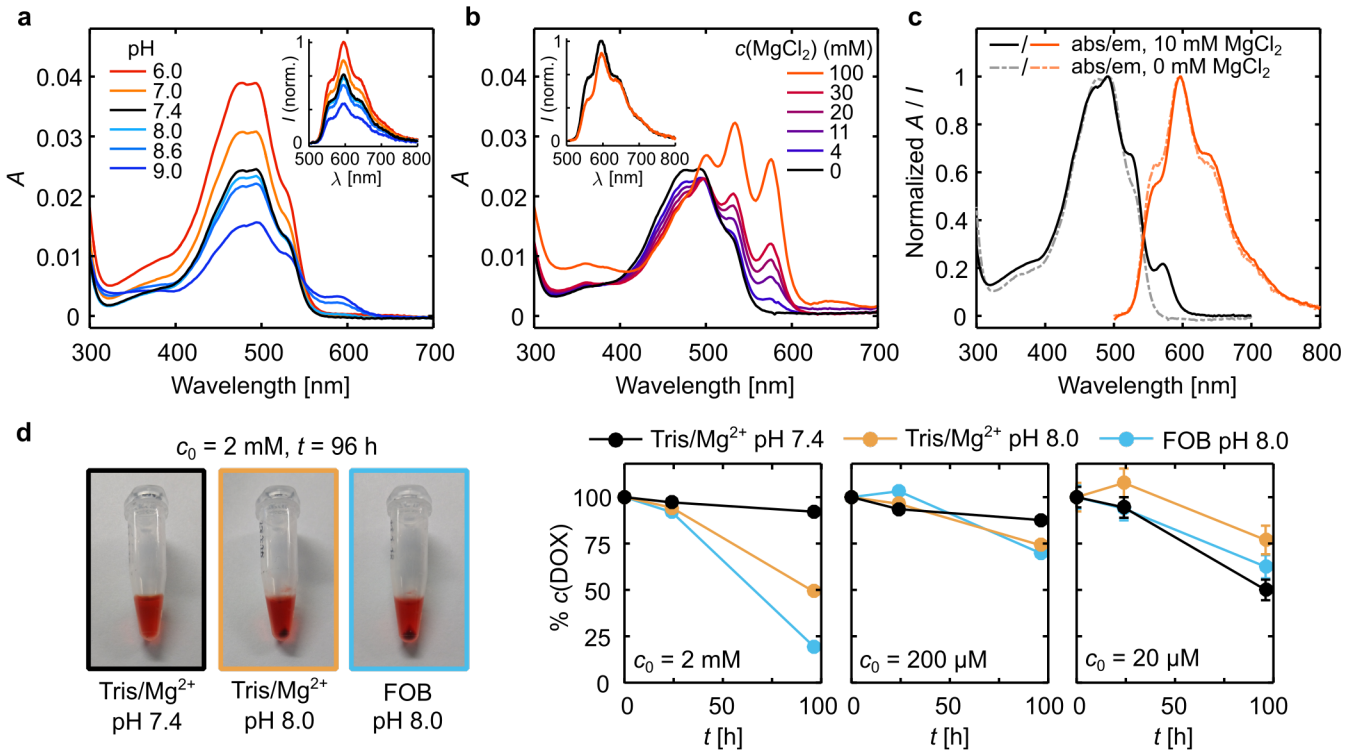

Figure 2. Effects of buffer conditions on the properties of the DOX in the absence of DNA. **a** Absorption and emission (inset) spectra of 3 μM DOX in 40 mM Tris, 0 mM $MgCl_2$ at pH 6.0–9.0. The emission spectra were obtained at an excitation wavelength of 494 nm. **b** Absorption and fluorescence emission (494 nm excitation) of 3 μM DOX in 40 mM Tris, pH 7.4 buffer at different $MgCl_2$ concentrations. The inset figure shows a comparison of the emission spectra of the 0 mM and 100 mM samples, with the maximum emission intensity of the 0 mM $MgCl_2$ sample normalized to 1. The 0 mM $MgCl_2$ spectrum (black) corresponds to the pH 7.4 spectrum in Figure a. **c** Absorption and emission spectra of 3 μM DOX in the chosen experimental conditions – 40 mM Tris, 10 mM $MgCl_2$, pH 7.4. The effect of 10 mM $MgCl_2$ concentration is shown by comparing the spectra measured at 10 mM $MgCl_2$ concentration (solid lines) with spectra measured at 0 mM $MgCl_2$ (dashed lines). **d** Precipitation of DOX driven by high DOX concentration (mM scale), high pH (8.0), and increasing magnesium:DOX ratio (12.5 mM Mg^{2+} in FOB and 10 mM Mg^{2+} in both Tris/Mg^{2+} buffers, DOX concentration varies as indicated). The photographs on the left show the visible precipitation of 2 mM DOX in pH 8.0 buffers observed after 96 h incubation at RT and centrifugation at 14,000 g. The graphs on the right show the effect of the incubation time, total DOX concentration in the beginning of the incubation (c_0) and the applied buffer to the extent of self-aggregation and precipitation of DOX. The magnesium:DOX ratio in the samples increases from left to right with decreasing c_0. The concentration of DOX remaining in the supernatant (% *c*(DOX)) was quantified with absorbance (A_{480}) measurements.

at this absorption peak leads to a fluorescence spectral shape that is rather distinct from that of DOX in the absence of $MgCl_2$ (Supplementary Figure 2). While the emission spectrum of DOX at 0 mM $MgCl_2$ is homogeneous over the full absorption spectrum, the addition of $MgCl_2$ induces heterogeneity in the emission measurement reflected as the shape of the emission spectrum changing with the excitation wavelength (Supplementary Figure 2). As a result, the shape of the emission spectrum upon 494 nm excitation depends slightly on the $MgCl_2$ concentration (Figure 2b inset).

A comparison of the absorption and fluorescence spectra of 3 μM DOX in 40 mM Tris, pH 7.4 with either 0 mM or 10 mM $MgCl_2$ is shown in Figure 2c. The spectral differences indicate that at 10 mM $MgCl_2$, the sample and its absorption and fluorescence spectra are a combination of pure DOX and a small concentration of the DOX-Mg^{2+} complex. Despite the slight DOX heterogeneity in these conditions, 40 mM Tris at pH 7.4 supplemented with 10 mM $MgCl_2$ was chosen for all the experiments to maintain structural stability and integrity of the DNA origami.

DOX self-aggregation in high-pH buffers and precipitation due to Mg^{2+} ions over time

We then tested whether the effects of pH and $MgCl_2$ observed as spectral changes can also change the behavior of DOX in an extent that could affect the outcome of DOX - DNA origami experiments. In particular, the combined effect of pH and the applied DOX concentration can be expected to be large: near and above the pK_a of the NH_3^+ group, the solubility of the uncharged form of DOX is only 0.3 mg/mL (0.55 mmol/L; M = 543.52 g/mol), while the solubility of positively charged DOX in aqueous solution has been reported as 20 mg/mL (36.8 mmol/L) (50). In addition, high DOX concentrations can lead to dimerization (K_a = 1.4×10^4 M^{-1}) (47) or oligomerization of DOX (50). Nevertheless, DOX-loaded DNA origami structures are often prepared using DOX concentrations within the range of 1–2 mM at pH 8.0 or above (34, 36, 39, 41).

To characterize the effect of different experimental conditions, we studied the extent of self-aggregation of 20 μM to 2 mM DOX solutions prepared in three different buffers: in 40 mM Tris, 10 mM $MgCl_2$ at pH 7.4; in 40 mM Tris, 10 mM $MgCl_2$ at pH 8.0; and in a typical 2D DNA origami folding buffer (FOB) containing 1× TAE [40 mM Tris, 19 mM

bioRxiv preprint doi: https://doi.org/10.1101/2020.05.13.088054; this version posted May 15, 2020. The copyright holder for this preprint (which was not certified by peer review) is the author/funder. All rights reserved. No reuse allowed without permission.

acetic acid, 1 mM ethylenediaminetetraacetic acid (EDTA)] and 12.5 mM $MgCl_2$ at pH 8.0. After incubating the DOX solutions in the dark at room temperature, centrifugation was used to separate the insoluble fraction of DOX formed during the incubation.

At 2 mM DOX concentration, the choice of buffer shows a significant effect on the extent of DOX precipitation during incubation. After 96-hour incubation, centrifugation leads to a formation of a dark red DOX precipitate in both of the 2 mM DOX samples prepared in pH 8.0 buffers, but not in the pH 7.4 buffer (Figure 2d, photographs on the left panel). The observed DOX precipitation was further confirmed and quantified by determining the concentration of DOX in the supernatant from DOX absorbance (graphs in Figure 2d). At 2 mM DOX concentration in FOB, only 0.4 mM of DOX remains soluble after 96 hours. In Tris/Mg^{2+} at the same pH 8.0, but containing slightly less $MgCl_2$, the concentration of DOX in the supernatant is 1.0 mM. In the Tris/Mg^{2+} buffer at pH 7.4, aggregation is negligible with 1.8 mM of DOX found in the supernatant.

When the DOX concentration is decreased to 200 μM, *i.e.* below the solubility limit of the deprotonated DOX molecules, the differences between the buffers become smaller. However, when the relative amount of magnesium to DOX increases (from left to right in Figure 2d), DOX precipitation due to the apparent DOX-magnesium interaction starts to play a significant role. This effect is clearly seen at 20 μM DOX after a long-term storage. Comparison of the full absorption spectra of the samples likewise shows that the effect of Mg^{2+} on the shape of the spectra increases at lower DOX concentrations where the relative amount of magnesium is large (Supplementary Figure 3).

DOX loading

Next, we studied the interaction between DOX and five structurally distinct DNA origami nanostructures in the selected buffer conditions. The DNA origami structures include three 2D and two 3D DNA origami designs (Figure 3a): the Rothemund triangle (7), a bowtie (61), a double-L (61), a capsule (26), and a 24-helix bundle (24HB) (see Supplementary Figures 12–14 and Supplementary Table 5). The correct high-yield folding and structural integrity of all the DNA origami structures were verified with atomic force microscopy (AFM) or transmission electron microscopy (TEM) (Figure 3a).

Absorption and fluorescence properties of the DOX-DNA origami complexes. To study the DOX loading process in detail, we performed a set of titration experiments where the concentration of DOX was held constant at 3 μM while the concentration of DNA origami in the sample was increased. When the concentration of DNA in the sample increases over the titration, an increasing fraction of DOX binds to DNA, observed as changes in DOX light absorption and quenching of fluorescence. After addition of DNA, the samples were incubated for 2.5 min before the spectra were collected in order to reach an equilibrium where the amount of DOX bound to the DNA has stabilized. The 2.5 min incubation time was found to be sufficient, as no further spectral changes were observed over longer incubation times (Supplementary Figure 9), in accordance with existing literature where the equilibrium is reached within seconds (47).

The left panel of Figure 3b shows how the absorption spectrum of DOX changes upon titration with the triangle DNA origami. Binding to DNA causes a slight red-shift of the absorption spectrum and an overall decrease of ϵ in the visible wavelength region. Additionally, the absorption peak associated with the DOX-Mg^{2+} complex at *ca.* 570 nm disappears, when the stronger DOX-DNA interaction causes dissociation of the weakly bound DOX-Mg^{2+} complexes. The DOX fluorescence quantum yield (Φ) decreases upon DNA addition, as shown in the middle panel of Figure 3b for excitation wavelength 494 nm. The fluorescence spectra were corrected for the decrease of ϵ_{494}, which also leads to decreasing fluorescence intensity when less light is absorbed in the sample. By the end of the titration and at a base pair/DOX molar ratio of approximately 15, the titration is close to a saturation point with ϵ_{494} decreased by *ca.* 35%, and Φ *ca.* 89% (Figure 3b, right panel). The absorption and fluorescence spectra of bowtie, double-L, capsule, and 24HB DNA origami appear highly similar to the triangle DNA origami, and are presented in the Supplementary Figure 4.

Increasing the amount of DNA origami in the sample causes a discernible scattering effect, which is stronger for the 3D DNA origami shapes than for the 2D shapes (Supplementary Figure 10). In the absorbance measurement, this is observed as a slight elevation in the spectrum baseline during the titration, which has an influence on the apparent sample absorbance. While the scattering effect is minor compared to the spectral changes of DOX, it leads to moderately increased apparent ϵ of DOX in the end of the titration for the 3D shapes (Supplementary Figure 5). For this reason, further analysis of the binding was based on the fluorescence data, which is less affected by the light scattering effects. Analysis of the absorption data was then carried out using the parameters obtained from the analysis of the fluorescence data.

Interpretation of the experimental results through a molecular binding model. DOX has been proposed to bind dsDNA through two prevalent mechanisms: intercalation between G–C base pairs, and binding at A–T rich areas (47) *via* minor groove binding through electrostatic interactions, which is also considered an intermediate step in the intercalation process (46). The fluorescence of DOX has been shown to be fully quenched in the more strongly bound DOX-GC complex (intercalation), while the weaker DOX-AT complex remains gently fluorescent in double-stranded DNA (dsDNA) (47, 62). This is also fully supported by our observations; when DOX electrostatically binds to a single-stranded DNA (ssDNA), the DOX fluorescence does not quench, although its absorption spectrum changes in a similar fashion as in the case of DNA origami (Supplementary Figure 8). For describing the observed decrease of Φ and ϵ when increasing the concentration of DNA origami, we thus applied a 1:2 molecular binding model for including both modes of interaction and the formation of two distinct DOX-DNA complexes with different association constants (K_{11} and K_{12}) and fluores-

bioRxiv preprint doi: https://doi.org/10.1101/2020.05.13.088054; this version posted May 15, 2020. The copyright holder for this preprint (which was not certified by peer review) is the author/funder. All rights reserved. No reuse allowed without permission.

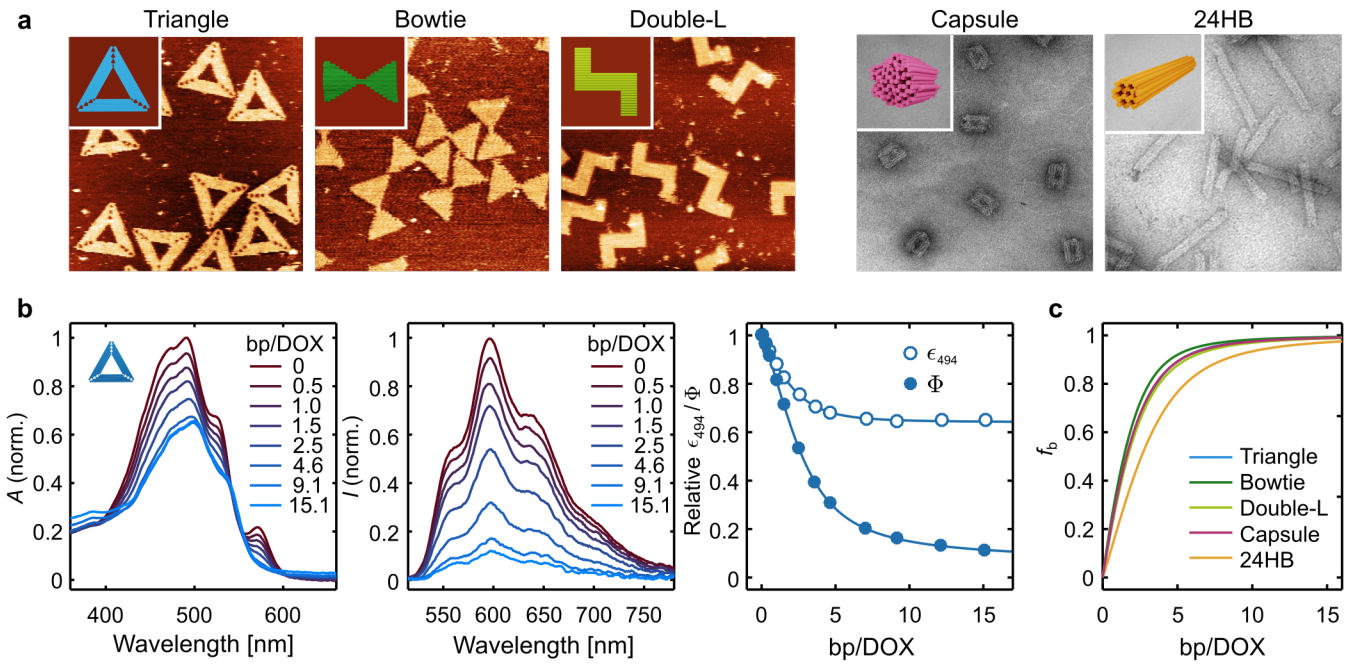

Figure 3. DNA origami titration experiments for determining the DOX-loading properties of different DNA origami structures. **a** The models and microscopy images of the studied 2D and 3D DNA origami. The triangle, bowtie, and double-L 2D DNA origami are shown on the left accompanied by atomic force microscopy (AFM) images. The 3D DNA origami – the capsule and the 24-helix bundle (24HB) are shown on the right in TEM images. The AFM images are 500 nm × 500 nm in size, and the TEM images are 300 nm × 300 nm. **b** Representative changes in the absorption spectrum (left panel) and fluorescence emission after 494 nm excitation (middle panel) of 3 μM DOX when the concentration of DNA base pairs (bp) in the solution is increased. The spectra have been measured for the triangle DNA origami after the system has reached equilibrium. The DNA concentration at each titration step is expressed as the molar ratio between DNA base pairs and DOX molecules in the sample (bp/DOX), and indicated in the legend. The fluorescence spectra in the middle panel have been corrected for the decrease of the molar extinction coefficient at the excitation wavelength (ϵ_{494}), and represent the quantum yield of the emitting molecules. The relative decrease of ϵ_{494} and Φ during titration with the triangle DNA origami are shown against the amount of DNA added (bp/DOX ratio) in the right panel. The measured values for ϵ_{494} and Φ have been fitted with a 2-component binding model as described in the text. The corresponding spectra and titration isotherms for the other DNA origami structures are presented in the Supplementary Figure 4. **c** Increase of the fraction of bound DOX molecules (f_b) when the DNA base pair concentration in the sample increases, obtained by fitting the fluorescence data.

cence quantum yields (Φ_{11} and Φ_{12}).

In the right panel of Figure 3b, the dependence of Φ and ϵ_{494} on the base pair concentration in the triangle DNA origami sample is described by a fit according to Equations (2) and (4) [Equations (1–7) can be found in the Materials and Methods section]. The model suggests that in the fluorescence measurement, the two DOX-DNA complexes with an average $K_{11} = (2.0 \pm 0.3) \times 10^5$ M^{-1} and $K_{12} = (2.6 \pm 0.2) \times 10^5$ M^{-1} can be differentiated from each other by the extent of fluorescence quenching ($\Phi_{11}/\Phi_0 = 0.52 \pm 0.07$ and $\Phi_{12}/\Phi_0 = 0.067 \pm 0.009$), but in terms of light absorbance, their physical properties are similar ($\epsilon_{11}/\epsilon_0 = 0.58 \pm 0.08$ and $\epsilon_{12}/\epsilon_0 = 0.67 \pm 0.09$ for 494 nm).

The binding model can thus be seen to present a reasonable approximation for the behavior of the system and the changes of the physical properties of DOX (Φ and ϵ) upon DNA addition by taking into account the two types of binding modes, and essentially, their distinct fluorescence properties. The determined values of K_{11} and K_{12} are in the same range and order of magnitude as in previous studies (47, 62) – nevertheless, we note that generalization of the fitting results and the obtained parameters outside the presented experimental conditions should be carried out with caution due to the simplifications of the model. A comparison of the fitting parameters for all DNA origami structures presented in this study can be found in the Supplementary Table 2.

The fraction of bound DOX molecules at each bp concentration can then be obtained from the fit according to Equation (3), which enables a comparison of the DOX loading properties for different kinds of DNA origami shapes (Figure 3c). It appears that the DNA origami superstructure has relatively little effect on how much DOX can be bound to the structures, as all curves in Figure 3c are rather similar. In the beginning of the titration, the fraction of bound DOX increases sharply when DNA is introduced into the sample. The maximum number of bound DOX molecules per base pair is reached at 0.36 ± 0.10 (Supplementary Figure 6).

DOX release upon nuclease degradation

After determining that all the studied DNA origami shapes have rather similar DOX loading capacity, we studied their superstructure-related differences towards DNase I digestion. When the DOX-loaded DNA origami structures are digested by DNase I, the dsDNA structure of the DNA origami breaks down as the nuclease cleaves the DNA into short ssDNA fragments. As the ϵ_{260}/nt for ssDNA is higher than the ϵ_{260}/nt for dsDNA (63), the process can be followed from the increase of the A_{260} of the sample. The bound DOX is released when the double-helical DNA structure unravels, observed as a recovery of DOX fluorescence. In order to follow both processes in detail, we employed a simultaneous kinetic spectroscopic characterization of both the increase of DNA absorbance and

bioRxiv preprint doi: https://doi.org/10.1101/2020.05.13.088054; this version posted May 15, 2020. The copyright holder for this preprint (which was not certified by peer review) is the author/funder. All rights reserved. No reuse allowed without permission.

the recovery of DOX fluorescence during DNase I digestion in DOX-loaded DNA origami samples.

We studied the effect of the DOX loading content, which can be tuned with the DOX concentration during loading: at 3 μM DOX (molar ratio bp/DOX = 4.5 ± 1.5), the average density of DOX bound in the structures was determined as 0.20 ± 0.05 bound DOX molecules/bp, based on the measured DOX fluorescence quenching and parameters obtained for the thermodynamic DOX-DNA binding model. Doubling the DOX concentration to 6 μM (bp/DOX = 2.3 ± 0.8), while keeping the concentration of DNA base pairs constant, leads to a slightly higher number of bound DOX molecules; 0.33 ± 0.07 DOX/bp. It is noteworthy to acknowledge that free, unbound DOX in the solution was not removed before the digestion experiments, as this would disturb the binding equilibrium and promote an additional pathway of DOX release during the incubation. A comprehensive list of the bp/DOX ratios and amounts of loaded and free DOX in the samples can be found in the Supplementary Table 4.

When the DNA origami are digested by DNase I, the A_{260} of the samples increases roughly linearly, until reaching a saturation point where the structures are fully digested. Full digestion of the double-helices increases the A_{260} of the 2D structures on average by (30 ± 2)%, and the A_{260} of the 3D structures by (22 ± 4)%. Theoretical values predicted by calculating the ϵ_{260}/nt for intact and digested structures according to Equation 1 are (46 ± 3)% and (44 ± 5)% for 2D and 3D structures, respectively. The smaller measured values in comparison with the predicted values suggest the initial ϵ_{260}/nt values to be slightly overestimated for all DNA origami structures, and more so for 3D structures that cause more light scattering in the intact state (see Supplementary Figure 10).

Following the A_{260} increase of the DNA origami reveals that the dsDNA structure of the DNA origami breaks down at distinct rates depending both on the DNA origami superstructure and the DOX concentration in the sample (Figure 4a). In general, both 3D shapes are digested more slowly than the 2D structures, and their digestion profiles are thus presented over 41 hour incubation, while a shorter (< 1 h) incubation is sufficient for studying the DNase I digestion of the 2D structures. The fastest digestion is observed for the triangle DNA origami in the absence of DOX, with the structures being completely degraded within 20 minutes of incubation in the presence of 34 U/mL DNase I. Notably, increasing amounts of DOX slow down the DNase I digestion by a considerable extent. The digestion rates of all structures are compared in Figure 4d, where the effect of slightly different DNase I concentrations for the 2D and 3D structures has been taken into account by normalizing the rates per unit of DNase I.

To further support the spectroscopic results of the DNA origami digestion, an agarose gel electrophoresis (AGE) analysis was carried out parallel to the kinetic DNA absorption and DOX fluorescence measurements (Figure 4b). Incubating the 24HB and the capsule with 28 U/mL DNase I leads to a lower band intensity and an increased electrophoretic mobility of the samples, indicating a reduced size of the partly digested DNA origami. In the case of complete digestion, the bands disappear completely. The observed effects of DNase I digestion in AGE after 17 h and 41 h are well in agreement with the structural digestion determined from the A_{260} increase in Figure 4a. Likewise, incubating the 2D structures for 17 h in the same conditions as for the 3D structures leads to complete digestion of the structures, observed both as a stabilized A_{260} signal and a disappearance of the DNA origami bands in AGE (Supplementary Figure 11).

When DOX-loaded DNA origami are digested by DNase I, DOX release is observed as a recovery of DOX fluorescence. Figure 4a presents the fraction of initially loaded DOX molecules released from the DNA origami during the DNase I incubation. For both DOX concentrations, the fractions of bound and released DOX are closely linked to the fraction of intact dsDNA residues in the samples. As a result, the total amount of loaded DOX is released more slowly from the 6 μM DOX samples than from the 3 μM DOX samples. The cross-correlation between released DOX and the intactness of the DNA origami structures for the 3 μM DOX samples is shown in Figure 4c.

While the 6 μM DOX samples are digested more slowly, they also contain a higher amount of DOX than the less densely loaded 3 μM DOX samples. When the loading density of the structures is taken into account and the DOX release is considered in terms of the absolute number of released DOX molecules, the difference between the DOX release properties of 3 μM and 6 μM DOX samples decreases. In Figure 4e, the DOX release rates are compared in terms of the number of DOX molecules released per unit of time per unit of DNase I. The general trend observed for the different structures is that while the 6 μM samples are able to release more DOX into the solution, the inhibition of DNase I function is still a stronger effect and leads to faster drug release rates from the 3 μM samples.

Discussion

DOX loading and choice of conditions

In common experimentation with DNA origami, the buffer of choice is typically a Tris-HCl or a TAE buffer, either supplemented with on average 10–20 mM Mg^{2+}. These conditions have been generally found to be appropriate for stabilizing the DNA origami structures: the divalent cations effectively screen the electrostatic repulsion between the negative charges of closely packed phosphate backbones, and the typical pH at 8.0–8.3 is in the optimal buffering range of Tris-based buffers. As it is important to retain the structural integrity of DNA origami nanostructures throughout experimental procedures, these conditions are also commonly used together with DOX – particularly during incorporating (loading) the DOX into the DNA origami structures. Still, the question of whether these conditions can cause unexpected or undesired behavior of DOX, or change its spectroscopic properties in terms of ϵ or Φ in a way that can lead to a misinterpretation of spectroscopic observables, has been left almost entirely unaddressed.

bioRxiv preprint doi: https://doi.org/10.1101/2020.05.13.088054; this version posted May 15, 2020. The copyright holder for this preprint (which was not certified by peer review) is the author/funder. All rights reserved. No reuse allowed without permission.

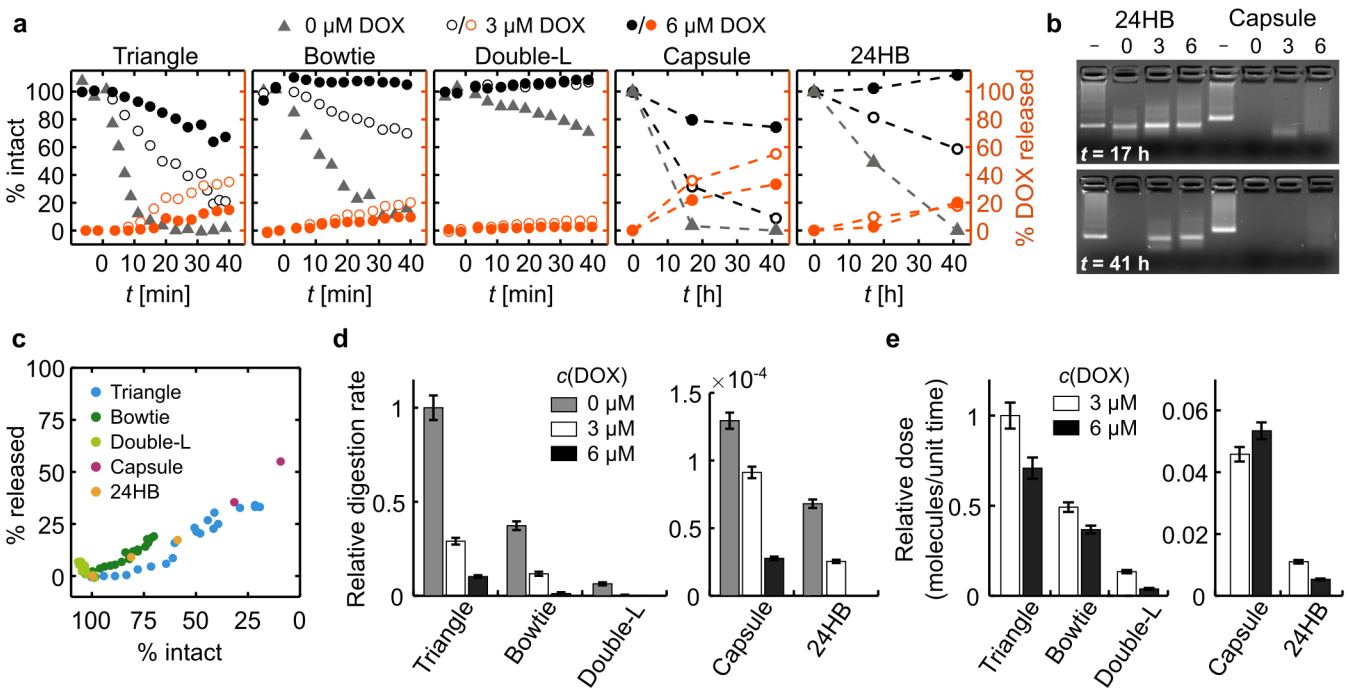

Figure 4. Digestion of the DNA origami nanostructures and DOX release during incubation with DNase I. **a** Comparison of the degradation of the dsDNA framework of the DNA origami shapes and the resulting DOX release. The structural integrity of the DNA origami (% intact), as determined from the increase of the A_{260} signal, is shown with the gray triangle markers for the samples without DOX, and with the empty and filled black markers for the samples containing DOX at either 3 or 6 μM concentration. For the samples with 3 and 6 μM DOX, the orange markers depict the fraction of released DOX molecules relative to the initial concentration of bound DOX molecules. **b** Agarose gel electrophoresis (AGE) analysis of the 24HB and capsule DNA origami samples after 17 h and 41 h digestion. The first lane for each sample (-) contains the DNA origami without DNase I or DOX; the lanes marked with 0, 3, and 6 contain the indicated concentration of DOX in μM, with additional 28.2 U/mL of DNase I in each sample. **c** Cross-correlation plots of % DOX release *vs.* % intact for all DNA origami shapes at 3 μM DOX. **d** DNase I digestion rates relative to the rates measured for the triangle DNA origami. DNase I digestion rate denotes the decrease rate of the relative fraction of intact dsDNA structures. **e** Relative dose stands for the number of DOX molecules released per unit of time and takes into account the absolute concentration of DOX molecules loaded into the DNA origami in the beginning of the incubation. Both the digestion and release rates have been normalized to the concentration of DNase I in the samples (34 U/ml for the triangle, bowtie, and double-L, and 28 U/mL for the 24HB and the capsule), and further shown relative to the rates measured for the triangle DNA origami.

In our spectroscopic analysis, we found that if the pH is at or above 8.0 and the $MgCl_2$ concentration is at mM range, the environment will lead to DOX heterogeneity either in terms of charge (deprotonation) or formation of DOX-Mg^{2+} complexes (Figure 2a-c). In general, the spectroscopic properties of DOX are obviously associated with the prevalent solution pH, but unfortunately this fact is often brushed aside (34, 40). For example, it has been stated that the amount of DOX released from the DNA structures increases with decreasing pH (34), but our results strongly suggest that the observed elevation in DOX absorbance and fluorescence may just arise from the spectroscopic properties of DOX (high absorbance and emission at low pH) and not from the DOX concentration change.

While the observations are important for validating the spectroscopic results obtained at these buffer conditions, they also reflect the aggregation behavior of DOX observed in different Tris-based buffers supplemented with $MgCl_2$ (Figure 2d). The precipitation of DOX during storage at RT indicates two major aggregation pathways in line with the previous literature (47, 50, 58, 59). The more prevalent one is observed at pH $\geq$ 8.0 when the DOX concentration is above the solubility of the deprotonated molecules (0.55 mmol/L) (50). The second mechanism is linked to the complexation with Mg^{2+}, which causes slight DOX aggregation and precipitation regardless of the DOX concentration (from μM to mM range). This aggregation pathways becomes notable at lower DOX concentrations where the magnesium:DOX ratio is high and the contribution of the more significant aggregation mechanisms is smaller.

The experimental conditions and the protocol of plain DOX incubation used here are consistent with the commonly used strategies to load DOX into DNA nanostructures (34, 36, 44). Incubation of DOX alone at millimolar concentrations and at pH 8.0 leads to an almost identical precipitate as using the reported DOX-loading approaches. Therefore, it is fairly reasonable to assume that the method for preparing purified DOX-loaded DNA origami structures *via* the same precipitation protocol (34, 36, 44) can likewise result in samples containing highly aggregated DOX.

Our results show that typical DNA origami buffers supplemented with $MgCl_2$ are not suited for unequivocal DOX experimentation. While the pH of the buffers can be readily adjusted to pH < 8.0, magnesium may be more challenging to exclude as it is a crucial counterion for screening the charged phosphate groups. While DNA origami have been shown to remain stable in low-Mg^{2+} conditions (55), addition of positively charged reagents such as DOX can be expected to influence the number of Mg^{2+} ions associated with the backbone in low-Mg^{2+} buffers, and thus may compromise the struc-

bioRxiv preprint doi: https://doi.org/10.1101/2020.05.13.088054; this version posted May 15, 2020. The copyright holder for this preprint (which was not certified by peer review) is the author/funder. All rights reserved. No reuse allowed without permission.

tural stability.

In summary, these findings may be used as a cautionary tale on how to choose the conditions for DOX loading. Certain compromises are inevitable and required for fitting together DNA origami and DOX, which both have a different optimal environment. According to our results, it is important to acknowledge the effect of these concessions in the loading process as well as in long-term drug release and storage.

DOX loading – efficiency and features

When DNA origami structures are mixed with DOX, the high DNA-binding affinity of the drug leads to a fast formation of non-covalently bound DNA origami-drug complexes. In our titration experiments, we studied and compared the DOX-loading capacities of five distinct DNA origami structures. In our experimental conditions and in the loading experiments presented in Figure 3, the maximum DOX loading content was determined to be 0.36 ± 0.10 DOX molecules bound per one DNA base pair. The value is in line with a number of previous studies for calf thymus dsDNA, where the maximum binding efficiency of DOX had been determined to be in the range of ∼0.29–0.37 DOX molecules per base pair (47, 64).

The association of DOX with DNA has been shown to take place predominantly *via* intercalation and minor-groove binding through electrostatic interactions. As intercalation is known to affect the DNA helicity and cause torsional twist in DNA origami structures (35, 65), we further elucidated the intercalation effect with the double-L structure and an atomic force microscopy (AFM) -based characterization. AFM images of DOX-loaded double-L DNA origami (see Supplementary Figure 7) show that although the double-L is designed to be in a *trans*-form (arms on the opposite sides of the middle bar), the DOX binding can twist it to a *cis*-form (arms on the same side of the middle bar) in a concentration-dependent manner. Importantly, all the structures remain intact upon DOX addition. Our results also strongly support the presence of a minor-groove binding mode that leads to a lesser extent of DOX fluorescence quenching (47, 62). It is thus highly likely that both modes of binding contribute to the loading capacity of the DNA origami structures in our experimental conditions.

Interestingly, roughly identical amounts of DOX were incorporated into all of the tested DNA origami shapes in terms of density of the drug molecules on the DNA – the DOX loading capacity of the DNA origami being thus only affected by the size of the structures in base pairs, and not by other design-related features. This is a rather surprising observation, as the steric hindrance from the compact arrangement of DNA helices could be expected to lead to a restricted accessibility of DNA helices and intercalation sites on the DNA origami, and particularly so for the 3D structures. In fact, such kind of restricted loading has recently been observed for the bis-intercalator YOYO-1 (49). The different behavior we observe for DOX might arise from the different binding mechanisms of the two drugs. Some subtle differences between the studied structures might have also been left undetected by our analysis methods.

Although our observations of low DOX-loading capacity of DNA origami are in agreement with the earlier dsDNA data, they seem to contradict many previous studies on DNA origami-based DOX delivery, where the reported concentrations of bound drug molecules in DNA origami structures are often higher than the concentration of DNA base pairs in the sample. For instance, the amount of DOX bound by the triangle DNA origami has been reported to range from 2.8–19 DOX molecules per base pair (37, 39, 41) to as high as 55 DOX molecules per base pair (34, 36).

While it is rather obvious that intercalation cannot be the only DOX binding mechanism behind the reported high DOX loading contents, the other possible processes, such as minor-groove binding or even external aggregate formation through stacking interactions (47), are rarely discussed. Our results support the interpretation that all three mechanisms might play a role in the loading process depending on the choice of experimental conditions, with DOX aggregation presenting a plausible explanation for DOX loading contents well above a loading density of DOX/bp > 1. Indicated *e.g.* by the previously reported long loading times and strategies, as well as by the kinetics in both *in vitro* and *in vivo* experimentation, the observed therapeutic effects could likewise be linked to DOX aggregates with only little or no contribution from the well-formed DOX-DNA origami complexes (34, 36, 37, 41, 42). As a result, the actual mechanism of anticancer action and therapeutic efficacy of these DOX-DNA origami samples without any DOX-loading optimization remains still unknown.

DNase I digestion leads to DOX release at superstructure-dependent rates

As an important prerequisite for any biomedical application, we simulated the possible degradation pathways of the complexes in DNase I-rich environments. DNase I was selected as a degradation agent as it is the most important and active nuclease in blood serum and mammalian cells. In addition, DNA nanostructure digestion by DNase I have been previously studied (52, 54, 66–69), but not with this kind of approach that allows monitoring of DNA origami cleavage and drug release simultaneously.

By following the change of DNA absorbance at 260 nm upon DNase I addition, it is possible to resolve superstructure-dependent DNA origami degradation rates. The stability varies from structure to structure, which has also been observed in the previous studies. In general, DNA origami structures are known to be more resistant toward DNase I digestion than plain dsDNA, and it seems that the rigid, closely packed helices and the strand routing play a role in the achieved resiliency (52, 54, 66, 68, 69). DNase I is a strong minor-groove binder (70). Its mechanism of action induces widening of the minor groove and a bending toward the major groove, thus making the flexible regions of DNA molecules and structures more susceptible towards cleavage (52, 70). Along with the increasing compactness and rigidity of DNA origami, the possible cleavage sites become less accessible (53). Recently, it was also found out that the stability

bioRxiv preprint doi: https://doi.org/10.1101/2020.05.13.088054; this version posted May 15, 2020. The copyright holder for this preprint (which was not certified by peer review) is the author/funder. All rights reserved. No reuse allowed without permission.

is DNA crossover-dependent (69).

The superstructure-dependent DNA origami digestion is notably slower for 3D than 2D structures; in the most extreme case (triangle *vs*. 24HB), by roughly four orders of magnitude (Figure 4a and 4d). However, the percentage of released DOX correlates well with the degradation level of the DNA origami (Figure 4c), thus enabling customized drug release over a rather wide time window. The plain 2D structures follow similar digestion profiles as reported earlier (52), and the increased stability of the 24HB compared to the capsule may originate from design features such as a more compact and regular structure and higher amount of scaffold crossovers. However, here it is noteworthy that when the structures are loaded with DOX, the digestion slows down and adds one more controllable parameter to the tunable release profile. The underlying mechanism is most likely DOX-induced DNA protection, which has also been previously observed for dsDNA with variable sequences (71). In other words, the bound DOX partially interferes with the minor-groove binding of DNase I.

Furthermore, to achieve reasonable time scales for the digestion rate comparison, we have here applied a DNase I concentration ($\sim$30 U/mL) that is remarkably higher than for example in blood plasma (0.36 $\pm$ 0.20 U/mL (72)). Obviously, DNase I concentration is not the only factor that affects the digestion rate, as the DNase I activity is also dependent *e.g.* on the buffer, salt concentration and temperature. However, as the concentration of DNase is essentially defined through its activity, the acquired results set an appropriate starting point to estimate the susceptibility and the drug release capacity of distinct DNA shapes. For that, the calculated relative dose (released amount of DOX / unit time) for each structure serves as a feasible measure of the actual release efficacy (Figure 4e). Interestingly, 6 μM DOX loading yields lower doses than 3 μM, however, in this setting the shape/structure of DNA origami plays a more crucial role. In a nutshell, the distinct DNA shapes used in this work and the applied DOX-loading levels together provide a broad selection of relative doses for fully engineered DOX delivery (Figure 4e).

Conclusions

We have shown that the release of the common therapeutic drug DOX from DNA nanostructures upon DNase I digestion can be customized by rationally designing DNA superstructures and adjusting the concentration of DOX. Importantly, our spectroscopic analysis of DOX-loaded DNA origami and free DOX under different conditions reveals that a number of studies have poorly estimated DOX loading capacity and overlooked the effect of DOX self-aggregation, which both may lead to suboptimal loading, questionable outcomes and misleading interpretation of the actual drug efficacy. Therefore, our results may also help in explaining previous, often incoherent reports on DNA origami-mediated DOX delivery.

Our results show that both the superstructure and rigidity of DNA origami have an impact on its stability against nucleases, which is in agreement with previous studies (52, 54, 66, 68). The stiffness and resilience of DNA origami achieved by the close packing of helices may, on the other hand, deteriorate the loading capacity of DNA-binding drugs (49). Nevertheless, here we observed nearly identical DOX loading properties for all DNA origami shapes, but drastically different digestion and release profiles. Interestingly, increasing the amount of loaded DOX slows down the digestion, which is plausibly associated with restricted DNase I cleavage due to the interfering DNA-bound DOX.

All of our observations underline the significant potential of DNA origami structures in drug delivery applications. Here we employed plain DNA origami without further modifications, but by taking advantage of their unsurpassable addressibility and modularity, multifunctionalities can be further realized. In the bigger picture, we believe our findings will help in building a solid ground for the development of safe and more efficient DNA nanostructure-based therapeutics with promising programmable features.

Materials and methods

Materials

Doxorubicin hydrochloride (HPLC-purified, Sigma-Aldrich) was dissolved in Milli-Q water for a 10 mM stock solution, divided into aliquots and stored at -20 °C. After thawing, the stock solution was stored at +4 °C and used within 2–3 days.

DNase I was purchased from Sigma-Aldrich. A stock solution was prepared at 2 U/μL concentration in deionized water and stored in aliquots at -20 °C, and after thawing used within the same day.

The staple oligonucleotides for DNA origami folding were purchased from Integrated DNA Technologies. For the Rothemund triangle (7), bowtie (61), double-L (61), and the closed capsule (26), the staple strand sequences and folding protocols were adopted from the original publications. The 24-helix bundle (24HB) was designed using caDNAno (73) and its shape was predicted using CanDo software (66, 74). The design of the 24HB structure is presented in the Supplementary Figures 12–14, and its staple strand sequences in the Supplementary Table 5. The self-assembly reaction for the 24HB was carried out in a buffer containing 1× TAE and 17.5 mM $MgCl_2$. The reactions were heated to 65 °C, and assembled by first cooling to 59 °C with a rate of 1 °C/15 min and then to 12 °C with rate 0.25 °C/45 min. All DNA scaffold strands were purchased from Tilibit Nanosystems at 100 nM concentration. The 7,249 nt long M13mp18 scaffold was used for folding the triangle, bowtie and double-L. The extended 7,560 nt and 8,064 nt variants were used for folding the 24HB and capsule, respectively. After thermal annealing, the DNA origami structures were purified of excess staple strands using polyethylene glycol (PEG) precipitation (75) in the presence of 7.5% (w/v) PEG 8000 (Sigma-Aldrich). After purification, DNA origami were resuspended in 40 mM Tris, 10 mM $MgCl_2$, pH 7.4 and incubated overnight at room temperature (RT) before use. The structural integrity was verified by AFM and TEM.

bioRxiv preprint doi: https://doi.org/10.1101/2020.05.13.088054; this version posted May 15, 2020. The copyright holder for this preprint (which was not certified by peer review) is the author/funder. All rights reserved. No reuse allowed without permission.

Spectroscopy techniques

Unless otherwise indicated, all UV-Vis absorption and fluorescence measurements were carried out with the Aqualog absorbance-fluorescence system (Horiba Scientific) operated with the Aqualog Software (v4.2) (Horiba Scientific), with the sample in a quartz cuvette with a 10 mm optical path length (Hellma Analytics). In spectral scans, a 3D excitation-emission matrix and the absorption spectrum of the sample were recorded simultaneously using an excitation light scan at 2 nm increments between 240–700 nm with 5 nm slit width. The emission spectrum for each excitation wavelength was collected between 245.16–827.17 nm at 1.16 nm increments with the CCD array. All measurements were performed at RT.

Free DOX characterization

Spectroscopic analysis of the effect of pH and $MgCl_2$ concentration. For measuring the effect of buffer pH on the spectroscopic properties of DOX, 40 mM Tris-HCl buffers at pH 6.0, 7.0, 7.4, 7.8, 8.0, 8.2, 8.6, or 9.0 were prepared by dissolving the required amount of Tris base in water and adjusting the pH of the solution with 1 M HCl. 3 μM DOX solutions were prepared in each of the buffers from the 10 mM stock solution and the UV-Vis absorption and 3D excitation-emission matrices of all samples were measured separately. The 3 μM DOX concentration was selected for avoiding possible DOX aggregation and self-quenching at high concentration, but also for performing accurate spectroscopic analysis in the low A (< 0.1) region where both A and emission intensity (I) values exhibit linear dependency on the concentration of the studied molecules.

For the measurement of DOX absorption and fluorescence in the presence of different $MgCl_2$ concentrations, 3 μM solutions of DOX were prepared in 40 mM Tris-HCl buffers at pH 7.4 at both 0 mM and 100 mM $MgCl_2$ concentration. The absorption and fluorescence spectra of both samples were first recorded separately as described. The 3 μM DOX in the 100 mM $MgCl_2$ buffer was then added in small volumes into the 3 μM DOX solution in the cuvette. After each addition, the sample was mixed by vortexing and its absorption and fluorescence spectra were recorded. The $MgCl_2$ concentration at each titration step was calculated according to the added volume of the 100 mM $MgCl_2$ DOX solution.

DOX self-aggregation in different buffer conditions. 2 mM, 200 μM and 20 μM dilutions of DOX were prepared in each of the three tested buffers: 1) 40 mM Tris with 10 mM $MgCl_2$, pH 7.4, 2) 40 mM Tris with 10 mM $MgCl_2$, pH 8.0, and 3) 1× TAE with 12.5 mM $MgCl_2$ (1× FOB), pH 8.0. In order to avoid diluting the buffer when preparing the DOX solutions by adding a relatively large volume of the 10 mM stock solution of water, the buffer concentration was always adjusted to the final 1× concentration with a concentrated buffer stock solution.

The UV-Vis absorption spectra of the solutions were measured in the beginning of the incubation using either a Cytation 3 cell imaging multi-mode reader (BioTek) on a Take3 plate with a 0.5 mm path length (2 mM and 200 μM samples), or Nanodrop ND-1000 with a 1 mm light path length (20 μM samples). After 24 h or 96 h incubation in dark at RT, the samples were centrifuged for 10 min at 14,000 g to separate the fraction of insoluble DOX. The concentration of DOX in the supernatant was determined by measuring the UV-Vis absorption similarly as in the beginning of the incubation. The relative decrease of the A_{480} value was used to calculate the decrease of DOX concentration relative to $t = 0$.

DNA origami - DOX titrations

UV-Vis and fluorescence spectroscopy. Association of DOX with DNA origami structures was studied by titrating a solution of 3 μM DOX in 40 mM Tris, 10 mM $MgCl_2$, pH 7.4 with a solution containing *ca.* 40 nM DNA origami (triangle, bowtie, double-L, capsule, or 24HB) and 3 μM DOX in the same buffer. 40 nM DNA origami concentration corresponds to 558–605 μM base pair concentration depending on the DNA origami design (see details in Supplementary Table 1). After each addition of the titrant, the sample was mixed by vortexing and let to equilibrate for 2.5 min before measuring the absorption and fluorescence spectra.

Data analysis and fitting. The concentration of DNA (total nucleotide concentration c(nt) at each point of the titration was determined from the DNA absorption at 260 nm (A_{260}). As both DNA and DOX absorb light at 260 nm, the contribution of DOX absorption was removed from the obtained A_{260} values by subtracting the A_{260} of 3 μM DOX collected in the beginning of the titration. c(nt) was determined according to the Beer-Lambert law. The molar extinction coefficient per nucleotide (ϵ_{260}/nt) was calculated separately for each DNA origami shape according to the number of unpaired nucleotides (N_{ss}) and number of hybridized nucleotides (N_{ds}) in the design with a formula adapted from Hung *et al.* (76),

$$\epsilon_{260}/\mathrm{nt} = \frac{6,700 \times N_{\mathrm{ds}} + 10,000 \times N_{\mathrm{ss}}}{N_{\mathrm{ds}} + N_{\mathrm{ss}}} \mathrm{M}^{-1}\mathrm{cm}^{-1}. \quad \textbf{(1)}$$

The values of N_{ss} and N_{ds} for each DNA origami design are presented in Supplementary Table 1. Only the concentration of hybridized nucleotides (base pair concentration $c(\mathrm{bp}) = 0.5 \times c(\mathrm{nt}) \times N_{\mathrm{ds}}/(N_{\mathrm{ds}} + N_{\mathrm{ss}})$) was taken into account in the analysis. Although all DNA origami shapes used in this work, except the triangle, contain single-stranded poly-T_8 extensions at the helix ends to prevent aggregation, their contribution to DOX quenching is negligible. This is a valid approximation, as non-interacting single-stranded DNA (ssDNA) quench DOX fluorescence only slightly when compared to the quenching caused by double-stranded DNA (dsDNA) (Supplementary Figure 8). In addition, the fraction of unpaired nucleotides (mostly the inert poly-T sequences) of the total number of nucleotides [$N_{\mathrm{ss}}/(N_{\mathrm{ds}} + N_{\mathrm{ss}})$] in the structures is small (0.4–12%). However, it is noteworthy that the staple mix solution alone quenches DOX efficiently, as the staple strands can partially hybridize or self-hybridize (see Supplementary Figure 8). Therefore, the purification of the structures from the excess staples after DNA origami folding is required for reliable quantification of DOX loading efficiency.

bioRxiv preprint doi: https://doi.org/10.1101/2020.05.13.088054; this version posted May 15, 2020. The copyright holder for this preprint (which was not certified by peer review) is the author/funder. All rights reserved. No reuse allowed without permission.

For fitting the fluorescence data, emission intensity values from 450, 460, 470, 480, and 494 nm excitation were obtained from the integrated emission spectra. The values were corrected for the extinction coefficient decrease during titration by dividing with $(1-T)$ for the excitation wavelength (T denotes the transmittance, obtained from the simultaneous absorption measurement). The corrected values thus represent the decrease of DOX fluorescence quantum yield (Φ) upon DNA binding. The dependence of Φ on c(bp) was fitted with a 1:2 host-guest binding model using the BindFit online fitting tool at https://supramolecular.org (77). The binding constants K_{11} and K_{12}, as well as Φ_{11} and Φ_{12} – the quantum yields of the two different DOX-DNA complexes with 1:1 and 1:2 DOX:base pair stoichiometries, respectively – were obtained from the fit. The fraction of bound DOX molecules f_b at each step of the titration was then determined as

$$f_\mathrm{b} := \frac{c(\mathrm{DOX})_\mathrm{b}}{c(\mathrm{DOX})_0} = 1 - \frac{1}{1+K_{11}c(\mathrm{bp})_\mathrm{ub}+K_{11}K_{12}c(\mathrm{bp})_\mathrm{ub}^2}, \quad \textbf{(2)}$$

where $c(\mathrm{DOX})_\mathrm{b}$ is the calculated bound DOX concentration, $c(\mathrm{DOX})_0$ denotes the total DOX concentration (3 μM) and $c(\mathrm{bp})_\mathrm{ub}$ is the concentration of unbound base pairs, *i.e.* the free base pairs not bound to DOX, obtained from

$$Ac(\mathrm{bp})_\mathrm{ub}^3 + Bc(\mathrm{bp})_\mathrm{ub}^2 + Cc(\mathrm{bp})_\mathrm{ub} - c(\mathrm{bp})_0 = 0, \quad \textbf{(3)}$$

$$\text{where} \begin{cases} A = K_{11}K_{12} \\ B = K_{11}[2K_{12}c(\mathrm{DOX})_0 - K_{12}c(\mathrm{bp})_0 + 1]. \\ C = K_{11}[c(\mathrm{DOX})_0 - c(\mathrm{bp})_0] + 1 \end{cases}$$

The molar extinction coefficients of the two DOX-DNA complexes, ϵ_{11} and ϵ_{12}, at wavelengths 450, 460, 470, 480, and 494 nm, were then determined with non-linear least-squares curve fitting with MATLAB R2015b to the equation

$$\Delta A_\mathrm{obs} = \frac{\epsilon_{\Delta 11}K_{11}c(\mathrm{bp})_\mathrm{ub}}{1+K_{11}c(\mathrm{bp})_\mathrm{ub}+K_{11}K_{12}c(\mathrm{bp})_\mathrm{ub}^2} + \frac{\epsilon_{\Delta 12}K_{11}K_{12}c(\mathrm{bp})_\mathrm{ub}^2}{1+K_{11}c(\mathrm{bp})_\mathrm{ub}+K_{11}K_{12}c(\mathrm{bp})_\mathrm{ub}^2}, \quad \textbf{(4)}$$

where ΔA_obs is the detected difference of the absorbance of the sample at the detection wavelength and the absorbance of 3 μM DOX in the absence of DNA. $\epsilon_{\Delta 11}$ and $\epsilon_{\Delta 12}$ are the differences between the molar extinction coefficient of free DOX and the molar extinction coefficients of the two complexes. K_{11}, K_{12}, and $c(\mathrm{bp})_\mathrm{ub}$ at each point of the titration were obtained from the analysis of the fluorescence data. The values for K_{11}, K_{12}, $\epsilon_{\Delta 11}$, and $\epsilon_{\Delta 12}$ for each DNA origami shape are listed in the Supplementary Table 2.

DNase I digestion of DNA origami

Kinetic UV-Vis and fluorescence measurements. The DNase I digestion and DOX release rates of the triangle, bowtie, and double-L DNA origami were determined with a simultaneous kinetic measurement of the A_{260} and DOX emission spectra (494 nm excitation) with the Horiba Aqualog absorbance-fluorescence system. Three samples were prepared of each DNA origami shape, each containing 2 nM DNA origami in 40 mM Tris, 10 mM $MgCl_2$, pH 7.4 and either no DOX, or with DOX added in a final concentration of 3 μM or 6 μM. The A_{260} and DOX emission of the sample were first recorded without DNase I. DNase I was then added to final concentration of 34 U/mL, the sample was briefly mixed by vortexing, and a kinetic measurement was started immediately.

The digestion and DOX release of the capsule and the 24HB were measured over 41 h incubation with DNase I. Samples containing 2 nM DNA origami with no DOX, 3 μM DOX, or 6 μM DOX were prepared for both DNA origami. The UV-Vis absorption spectra before DNase I addition were measured with Varian Cary 50 UV-Vis spectrophotometer. DOX fluorescence spectra between 490–700 nm were measured with a Cytation 3 cell imaging multi-mode reader (BioTek) from a 100 μL sample volume on a black 96-well plate (Costar) using 460 nm excitation. DNase I was then added in a 28 U/mL final concentration. The samples were incubated in dark at RT, and the UV-Vis absorption and fluorescence measurements were repeated after 17 h and 41 h incubation.

For both sets of kinetic measurements, control samples containing only 3 μM or 6 μM DOX and DNase I were measured similarly for obtaining references for the fluorescence quantum yield of free DOX in the same experimental conditions.

Data analysis of the kinetic measurements. The nuclease digestion of the DNA origami structures increases the A_{260} value of the samples. The percentage of intact dsDNA residues (% intact) at each time point was calculated as

$$\%\ \mathrm{intact} = \frac{A_{260}(t) - A_{260}(\mathrm{intact})}{A_{260}(\mathrm{digested}) - A_{260}(\mathrm{intact})} \times 100\% \quad \textbf{(5)}$$

where $A_{260}(t)$ is the A_{260} value detected at a time point t, $A_{260}(\mathrm{intact})$ is the A_{260} of fully intact structures measured before addition of DNase I, and $A_{260}(\mathrm{digested})$ is the A_{260} of fully digested structures, measured after the digestion has been completed (A_{260} value stabilized). For the data obtained from the 40 min incubation with DNase I, the initial DNase I digestion rates were determined by fitting a linear regression to the obtained % intact values *vs.* time with MATLAB R2015b. For the 41 h incubation data set, the digestion rate was calculated as the % intact difference between t = 17 h and t = 0, divided by the incubation time.

The analysis of DOX release from the DNA origami structures during DNase I digestion was based on the recovery of DOX quantum yield. The measured fluorescence emission intensities (from integrated spectra) of the 3 μM and 6 μM free DOX references and the DNA origami - DOX samples containing either 3 μM and 6 μM DOX were each corrected for the number of absorbed photons by dividing the intensities with $(1-T)$ for the excitation wavelength. The $c(\mathrm{bp})_\mathrm{ub}$ at each time point was solved from a modified and rearranged

bioRxiv preprint doi: https://doi.org/10.1101/2020.05.13.088054; this version posted May 15, 2020. The copyright holder for this preprint (which was not certified by peer review) is the author/funder. All rights reserved. No reuse allowed without permission.

version of Equation 4,

$$(K_{11}K_{12}\Delta\Phi_{\mathrm{obs}} - K_{11}K_{12}\Phi_{\Delta 12})c(\mathrm{bp})_{\mathrm{ub}}^2 + (K_{11}\Delta\Phi_{\mathrm{obs}} - K_{11}\Phi_{\Delta 11})c(\mathrm{bp})_{\mathrm{ub}} + \Delta\Phi_{\mathrm{obs}} = 0, \quad \textbf{(6)}$$

where $\Delta\Phi_{\mathrm{obs}}$ is the measured difference of the quantum yield of the DOX-DNA origami sample and the corresponding free DOX reference. $\Phi_{\Delta 11}$ and $\Phi_{\Delta 12}$ are the differences between the quantum yield of free DOX and the quantum yields of the 1:1 and 1:2 DOX-DNA complexes, respectively. K_{11}, K_{12}, $\Phi_{\Delta 11}$, and $\Phi_{\Delta 12}$ are fit parameters obtained from the titration experiments, and their values for each DNA origami shape are listed in the Supplementary Table 2. Knowing the $c(\mathrm{bp})_{\mathrm{ub}}$ at each time point, the mole fraction of bound DOX molecules at each time point $[f_{\mathrm{b}}(t)]$ was calculated with Equation 2. The percentage of released DOX (Figure 4a, c) was defined as

$$\%\ \mathrm{released} = \frac{f_{\mathrm{b}}(\mathrm{intact}) - f_{\mathrm{b}}(t)}{f_{\mathrm{b}}(\mathrm{intact})} \times 100\%, \quad \textbf{(7)}$$

where $f_{\mathrm{b}}(\mathrm{intact})$ is f_{b} of the sample before addition of DNase I. For calculating the DOX release rate in terms of relative dose per unit of time, the values for % released were multiplied by the DOX concentration bound to the DNA origami in the intact state. Release rates were calculated either by fitting a linear regression to the acquired values (40 min incubation) or as a difference between the t = 17 h and t = 0 time points (41 h incubation) similarly to the digestion rates, and normalizing the rate values to the concentration of DNase I in the sample.

Agarose gel electrophoresis (AGE). 2% agarose gels were prepared in 1× TAE, 11 mM $MgCl_2$, and pre-stained with ethidium bromide (0.47 µg/mL final concentration in the gel). The samples were loaded on the gel with loading dye (Sigma-Aldrich), run for 45 minutes at 90 V on an ice bath, and imaged with the BioRad ChemiDoc MP imaging system.

Microscopy imaging

Atomic force microscopy (AFM). To prepare the 2D DNA origami (triangle, bowtie and double-L) samples for AFM imaging, 10 µL of 3 nM DNA origami solution in 1× FOB (with 10 mM $MgCl_2$) was pipetted onto a fresh-cleaved mica sheet and incubated for 5 min. Then the mica substrate was washed 3 times with 100 µL ddH_2O by allowing it to flow from one end of the mica to the other and being blotted using a piece of cleanroom sheet. Finally, the sample was rigorously dried by pressurized N_2 gas. The AFM imaging was carried out using either a JPK NanoWizard ULTRA Speed with USCF0.3-k0.3 cantilevers (NanoWorld) in a liquid cell filled with 1× FOB (with 10 mM $MgCl_2$) or using a Bruker Dimension Icon instrument in Scanasyst air mode and Scanasyst-air probes.

Transmission electron microscopy (TEM). The 3D DNA origami samples (capsule and 24HB) were characterized using a Tecnai T12 TEM instrument. Copper TEM grids with both carbon and formvar films (FCF400-Cu from Electron Microscopy Sciences) were cleaned with O_2 plasma for 20 s, followed by pipetting 3 µL of 20 nM DNA origami solution on it and incubating for 2 min. Then the excess amount of solution was blotted with a piece of filter paper. To achieve better contrast, the sample was immediately stained with 20 µL of 2% uranyl formate for 40 s followed by blotting the staining solution with the filter paper. The grid was let to dry for at least 30 min before imaging.

Acknowledgements
This work was supported by the Academy of Finland (project 308578), the Emil Aaltonen Foundation, the Jane and Aatos Erkko Foundation, the Sigrid Jusélius Foundation, and the Vilho, Yrjö and Kalle Väisälä Foundation of the Finnish Academy of Science and Letters. The research was carried out under the Academy of Finland Centres of Excellence Programme (2014-2019). We thank H. Häkkänen for technical assistance and acknowledge the provision of facilities and technical support by Aalto University Bioeconomy Facilities and OtaNano – Nanomicroscopy Center (Aalto-NMC).

Author contributions
H.I. designed and performed the experiments, modeled the data and wrote the manuscript. B.S. and A.H.-J. designed and performed the experiments. A.K. conceived the project and designed the experiments. M.A.K., T.L. and J.A.I. supervised the work and designed the experiments. V.L. conceived and supervised the project, designed the experiments and wrote the manuscript. All authors analyzed and discussed the data and also commented on and edited the manuscript.

Additional information
Supplementary Information accompanies this paper.

Competing interests
The authors declare no competing interests.

References

1. Seeman, N. C. Nucleic acid junctions and lattices. *J. Theor. Biol.* **99**, 99, 237–247 (1982).
2. Jones, M. R., Seeman, N. C. & Mirkin, C. A. Programmable materials and the nature of the DNA bond. *Science* **347**, 1260901 (2015).
3. Hong, F., Zhang, F., Liu, Y. & Yan, H. DNA origami: Scaffolds for creating higher order structures. *Chem. Rev.* **117**, 12584–12640 (2017).
4. Nummelin, S., Kommeri, J., Kostiainen, M. A. & Linko, V. Evolution of structural DNA nanotechnology. *Adv. Mater.* **30**, 1703721 (2018).
5. Heuer-Jungemann, A. & Liedl. T. From DNA tiles to functional DNA materials. *Trends Chem.* **1**, 799–814 (2019).
6. Bathe, M. & Rothemund, P. W. K. DNA nanotechnology: A foundation for programmable nanoscale materials. *MRS Bull.* **42**, 882–888 (2017).
7. Rothemund, P. W. K. Folding DNA to create nanoscale shapes and patterns. *Nature* **440**, 297–302 (2006).
8. Andersen, E. S., Dong, M., Nielsen, M. M., Jahn, K., Subramani, R., Mamdouh, W., Golas, M. M., Sander, B., Stark, H., Oliveira, C. L. P., Pedersen, J. S., Birkedal, V., Besenbacher, F., Gothelf, K. V. & Kjems, J. Self-assembly of a nanoscale DNA box with a controllable lid. *Nature* **459**, 73–76 (2009).
9. Douglas, S. M., Dietz, H., Liedl, T., Högberg, B., Graf, F. & Shih, W. M. Self-assembly of DNA into nanoscale three-dimensional shapes. *Nature* **459**, 414–418 (2009).
10. Benson, E., Mohammed, A., Gardell, J., Masich, S., Czeizler, E., Orponen, P. & Högberg, B. DNA rendering of polyhedral meshes at the nanoscale. *Nature* **523**, 441–444 (2015).
11. Linko, V. & Kostiainen, M. A. Automated design of DNA origami. *Nat. Biotechnol.* **34**, 826–827 (2016).
12. Veneziano, R., Ratanalert, S., Zhang, K., Zhang, F., Yan, H., Chiu, W. & Bathe, M. Designer nanoscale DNA assemblies programmed from the top down. *Science* **352**, 1534 (2016).
13. Tikhomirov, G., Petersen, P. & Qian, L. Fractal assembly of micrometre-scale DNA origami arrays with arbitrary patterns. *Nature* **552**, 67–71 (2017).
14. Wagenbauer, K. F., Sigl, C. & Dietz, H. Gigadalton-scale shape-programmable DNA assemblies. *Nature* **552**, 78–83 (2017).
15. Castro, C. E., Dietz, H. & Högberg, B. DNA origami devices for molecular-scale precision measurements. *MRS Bull.* **42**, 925–929 (2017).
16. Pilo-Pais, M., Acuna, G. P., Tinnefeld, P. & Liedl, T. Sculpting light by arranging optical components with DNA nanostructures. *MRS Bull.* **42**, 936–942 (2017).
17. Xu, A., Harb, J. N., Kostiainen, M. A., Hughes, W. L., Woolley, A. T., Liu, H. & Gopinath, A. DNA origami: the bridge from bottom to top.

bioRxiv preprint doi: https://doi.org/10.1101/2020.05.13.088054; this version posted May 15, 2020. The copyright holder for this preprint (which was not certified by peer review) is the author/funder. All rights reserved. No reuse allowed without permission.

MRS Bull. **42**, 943–950 (2017).
18. Graugnard, E., Hughes, W. L., Jungmann, R., Kostiainen, M. A. & Linko, V. Nanometrology and super-resolution imaging with DNA. *MRS Bull.* **42**, 951–959 (2017).
19. Surana, S., Shenoy, A. R. & Krishnan, Y. Designing DNA nanodevices for compatibility with the immune system of higher organisms. *Nat. Nanotechnol.* **10**, 741–747 (2015).
20. Bujold, K. E., Lacroix, A. & Sleiman, H. F. DNA nanostructures at the interface with biology. *Chem* **4**, 495–521 (2018).
21. Hu, Q., Li, H., Wang, L., Gu, H. & Fan, C. DNA nanotechnology-enabled drug delivery systems. *Chem. Rev.* **119**, 6459–6506 (2019).
22. Keller, A. & Linko, V. Challenges and perspectives of DNA nanostructures in biomedicine. *Angew. Chem., Int. Ed.* **59**, DOI: 10.1002/anie.201916390 (2020).
23. Douglas, S. M., Bachelet, I. & Church, G. M. A logic-gated nanorobot for targeted transport of molecular payloads. *Science* **335**, 831–834 (2012).
24. Li, S., Jiang, Q., Liu, S., Zhang, Y., Tian, Y., Song, C., Wang, J., Zou, Y., Anderson, G. J., Han, J. Y., Chang, Y., Liu, Y., Zhang, C., Chen, L., Zhou, G., Nie, G., Yan, H., Ding, B. & Zhao, Y. A DNA nanorobot functions as a cancer therapeutic in response to a molecular trigger in vivo. *Nat. Biotechnol.* **36**, 258–264 (2018).
25. Grossi, G., Jepsen, M. D. E., Kjems, J. & Andersen, E. S. Control of enzyme reactions by a reconfigurable DNA nanovault. *Nat. Commun.* **8**, 992 (2017).
26. Iljäs, H., Hakaste, I., Shen, B., Kostiainen, M. A. & Linko, V. Reconfigurable DNA origami nanocapsule for pH-controlled encapsulation and display of cargo. *ACS Nano* **13**, 5959–5967 (2019).
27. Jiang, D., Ge, Z., Im, H.-J., England, C. G., Ni, D., Hou, J., Zhang, L., Kutyreff, C. J., Yan, Y., Liu, Y., Cho, S. Y., Engle, J. W., Shi, J., Huang, P., Fan, C., Yan, H. & Cai, W. DNA origami nanostructures can exhibit preferential renal uptake and alleviate acute kidney injury. *Nat. Biomed. Eng.* **2**, 865–877 (2018).
28. Lee, H., Lytton-Jean, A. K., Chen, Y., Love, K. T., Park, A. I., Karagiannis, E. D., Sehgal, A., Querbes, W., Zurenko, C. S., Jayaraman, M., Peng, C. G., Charisse, K., Borodovsky, A., Manoharan, M., Donahoe, J. S., Truelove, J., Nahrendorf, M., Langer, R. & Anderson, D. G. Molecularly self-assembled nucleic acid nanoparticles for targeted in vivo siRNA delivery. *Nat. Nanotechnol.* **7**, 389–393 (2012).
29. Schaffert, D. H., Okholm, A. H., Sørensen, R. S., Nielsen, J. S., Tørring, T., Rosen, C. B., Kodal, A. L., Mortensen, M. R., Gothelf, K. V. & Kjems, J. Intracellular delivery of a planar DNA origami structure by the transferrin-receptor internalization pathway. *Small* **12**, 2634–2640 (2016).
30. Halley, P. D., Lucas, C. R., McWilliams, E. M., Webber, M. J., Patton, R. A., Kural, C., Lucas, D. M., Byrd, J. C. & Castro, C. E. Daunorubicin-loaded DNA origami nanostructures circumvent drug-resistance mechanisms in a leukemia model. *Small* **12**, 308–320 (2016).
31. Kollmann, F., Ramakrishnan, S., Shen, B., Grundmeier, G., Kostiainen, M. A., Linko, V. & Keller, A. Superstructure-dependent loading of DNA origami nanostructures with a groove-binding drug. *ACS Omega* **3**, 9441–9448 (2018).
32. Thorn, C. F., Oshiro, C., Marsh, S., Hernandez-Boussard, T., McLeod, H. Klein, T. E. & Altman, R. B. Doxorubicin pathways: pharmacodynamics and adverse effects. *Pharmacogenet. Genom.* **21**, 440–446 (2011).
33. Pommier, Y., Leo, E., Zhang, H. & Marchand, C. DNA topoisomerases and their poisoning by anticancer and antibacterial drugs. *Chem. Biol.* **17**, 421–433 (2010).
34. Jiang, Q., Song, C., Nangreave, J., Liu, X., Lin, L., Qiu, D., Wang, Z. G., Zou, G., Liang, X., Yan, H. & Ding, B. DNA origami as a carrier for circumvention of drug resistance. *J. Am. Chem. Soc.* **134**, 13396–13403 (2012).
35. Zhao, Y.-X., Shaw, A., Zeng, X., Benson, E., Nyström, A. M. & Högberg, B. DNA origami delivery system for cancer therapy with tunable release properties. *ACS Nano* **6**, 8684–8691 (2012).
36. Zhang, Q., Jiang, Q., Li, N., Dai, L., Liu, Q., Song, L., Wang, J., Li, Y., Tian, J., Ding, B. & Du, Y. DNA origami as an in vivo drug delivery vehicle for cancer therapy. *ACS Nano* **8**, 6633–6643 (2014).
37. Song, L., Jiang, Q., Liu, J., Li, N., Liu, Q., Dai, L., Gao, Y., Liu, W., Liu, D. & Ding, B. DNA origami/gold nanorod hybrid nanostructures for the circumvention of drug resistance. *Nanoscale* **9**, 7750–7754 (2017).
38. Kang, J. H., Kim, K. R., Lee, H., Ahn, D. R. & Ko, Y. T. In vitro and in vivo behavior of DNA tetrahedrons as tumor-targeting nanocarriers for doxorubicin delivery. *Colloids Surf. B.* **157**, 424–431 (2017).
39. Zeng, Y., Liu, J., Yang, S., Liu, W., Xu, L. & Wang, R. Time-lapse live cell imaging to monitor doxorubicin release from DNA origami nanostructures. *J. Mater. Chem. B* **6**, 1605–1612 (2018).
40. Raniolo, S., Vindigni, G., Ottaviani, A., Unida, V., Iacovelli, F., Manetto, A., Figini, M., Stella, L., Desideri, A. & Biocca, S. Selective targeting and degradation of doxorubicin-loaded folate-functionalized DNA nanocages. *Nanomedicine* **14**, 1181–1190 (2018).
41. Liu, J., Song, L., Liu, S., Jiang, Q., Liu, Q., Li, N., Wang, Z.-G. & Ding, B. A DNA-based nanocarrier for efficient gene delivery and combined cancer therapy. *Nano Lett.* **18**, 3328–3334 (2018).
42. Liu, J., Song, L., Liu, S., Zhao, S., Jiang, Q. & Ding, B. A tailored DNA nanoplatform for synergistic RNAi-/chemotherapy of multidrug-resistant tumors. *Angew. Chem., Int. Ed.* **57**, 15486–15490 (2018).
43. Wiraja, C., Zhu, Y., Lio, D. C. S., Yeo, D. C., Xie, M., Fang, W., Li, Q., Zheng, M., Van Steensel, M., Wang, L., Fan, C. & Xu, C. Framework nucleic acids as programmable carrier for transdermal drug delivery. *Nat. Commun.* **10**, 1147 (2019).
44. Ge, Z., Guo, L., Wu, G., Li, J., Sun, Y., Hou, Y., Shi, J., Song, S., Wang, L., Fan, C., Lu, H. & Li, Q. DNA origami-enabled engineering of ligand-drug conjugates for targeted drug delivery. *Small* **16**, 1904857 (2020).
45. Wang, S.-T., Gray, M. A., Xuan, S., Lin, Y., Byrnes, J., Nguyen, A. I., Todorova, N., Stevens, M. M., Bertozzi, C. R., Zuckermann, R. N. & Gang, O. DNA origami protection and molecular interfacing through engineered sequence-defined peptoids. *Proc. Natl. Acad. Sci. USA* **117**, 6339–6348 (2020).
46. Lei, H., Wang, X. & Wu, C. Early stage intercalation of doxorubicin to DNA fragments observed in molecular dynamics binding simulations. *J. Mol. Graph. Model.* **38**, 279–289 (2012).
47. Pérez-Arnaiz, C., Busto, N., Leal, J. M. & García, B. New insights into the mechanism of the DNA/doxorubicin interaction. *J. Phys. Chem. B* **118**, 1288–1295 (2014).
48. Silva, E. F., Bazoni, R. F., Ramos, E. B. & Rocha, M. S. DNA-doxorubicin interaction: New insights and peculiarities. *Biopolymers* **107**, e22998 (2016).
49. Miller, H. L., Contrera, S., Wollman, A. J. M., Hirst, A., Dunn, K. E., Schröter, S., O'Connell, D. & Leakel, M. Biophysical characterisation of DNA origami nanostructures reveals inaccessibility to intercalation binding sites. *Nanotechnology* **31**, 235605 (2020).
50. Fülöp, Z., Gref, R. & Loftsson, T. A permeation method for detection of self-aggregation of doxorubicin in aqueous environment. *Int. J. Pharm.* **454**, 559–561 (2013).
51. Stopar, A., Coral, L., Di Giacomo, S., Adedeji, A. F. & Castronovo, M. Binary control of enzymatic cleavage of DNA origami by structural antideterminants. *Nucleic Acids Res.* **46**, 995–1006 (2018).
52. Ramakrishnan, S., Shen, B., Kostiainen, M. A., Grundmeier, G., Keller, A. & Linko, V. Real-time observation of superstructure-dependent DNA origami digestion by DNase I using high-speed atomic force microscopy. *ChemBioChem* **20**, 2818–2823 (2019).
53. Suma, A., Stopar, A., Nicholson, A. W., Castronovo, M. & Carnevale, V. Global and local mechanical properties control endonuclease reactivity of a DNA origami nanostructure. *Nucleic Acids Res.* **48**, gkaa080 (2020).
54. Hahn, J., Wickham, S. F. J., Shih, W. M. & Perrault, S. D. Addressing the instability of DNA nanostructures in tissue culture. *ACS Nano* **8**, 8765–8775 (2014).
55. Kielar, C., Xin, Y., Shen, B., Kostiainen, M. A., Grundmeier, G., Linko, V. & Keller, A. On the stability of DNA origami nanostructures in low-magnesium buffers. *Angew. Chem. Int. Ed.* **57**, 9470–9474 (2018).
56. Ramakrishnan, S., Iljäs, H., Linko, V. & Keller, A. Structural stability of DNA origami nanostructures under application-specific conditions. *Comput. Struct. Biotechnol. J.* **16**, 342–349 (2018).
57. Bila, H., Kurinsikal, E. E. & Bastings, M. M. C. Engineering a stable future for DNA-origami as a biomaterial. *Biomater. Sci.* **7**, 532–541 (2019).
58. Abraham, S. A., Edwards, K., Karlsson, G., MacIntosh, S., Mayer, L. D., McKenzie, C. & Bally, M. B. Formation of transition metal-doxorubicin complexes inside liposomes. *Biochim. Biophys. Acta - Biomembr.* **1565**, 41–54 (2002).
59. Cheung, B. C. L., Sun, T. H. T., Leenhouts, J. M. & Cullis, P. R. Loading of doxorubicin into liposomes by forming Mn^{2+}-drug complexes. *Biochim. Biophys. Acta - Biomembr.* **1414**, 205–216 (1998).
60. Jabłońska-Trypuć, A., Świderski, G., Krętowski, R. & Lewandowski, W. Newly synthesized doxorubicin complexes with selected metals - synthesis, structure and anti-breast cancer activity. *Molecules* **22**, 1106 (2017).
61. Shen, B., Linko, V., Tapio, K., Pikker, S., Lemma, T., Gopinath, A., Gothelf, K. V., Kostiainen, M. A. & Toppari, J. J. Plasmonic nanostructures through DNA-assisted lithography. *Sci. Adv.* **4**, eaap8978 (2018).
62. Airoldi, M. Barone, G., Gennaro, G., Giuliani, A. M. & Giustini M. Interaction of doxorubicin with polynucleotides. A spectroscopic study. *Biochemistry* **53**, 2197–2207 (2014).
63. Tinoco, I. Hypochromism in polynucleotides. *J. Am. Chem. Soc.* **82**, 4785–4790 (1960).
64. Barcelo, F., Martorell, J., Gavilanes, F. & Gonzalez-Ros, J. M. Equilibrium binding of daunomycin and adriamycin to calf thymus DNA: Temperature and ionic strength dependence of thermodynamic parameters. *Biochem. Pharmacol.* **37**, 2133–2138 (1988).
65. Chen, K., Zhang, H., Pan, J., Cha, T.-G., Li, S., Andréasson, J. & Choi, J. H. Dynamic and progressive control of DNA origami con-

bioRxiv preprint doi: https://doi.org/10.1101/2020.05.13.088054; this version posted May 15, 2020. The copyright holder for this preprint (which was not certified by peer review) is the author/funder. All rights reserved. No reuse allowed without permission.

formation by modulating DNA helicity with chemical adducts. *ACS Nano* **10**, 4989–4996.
66. Castro, C. E., Kilchherr, F., Kim, D.-N., Shiao, E. L., Wauer, T., Wortmann, P., Bathe, M. & Dietz, H. A primer to scaffolded DNA origami. *Nat. Methods* **8**, 221–229 (2011).
67. Conway, J. W., McLaughlin, C. K., Castor, K. J. & Sleiman, H. DNA nanostructure serum stability: greater than the sum of its parts. *Chem. Commun.* **49**, 1172–1174 (2013).
68. Auvinen, H., Zhang, H., Nonappa, Kopilow, A., Niemelä, E. H., Nummelin, S., Correia, A., Santos, H. A., Linko, V. & Kostiainen, M. A. Protein coating of DNA nanostructures for enhanced stability and immunocompatibility. *Adv. Healthcare Mater.* **6**, 1700692 (2017).
69. Chandrasekaran, A. R., Vilcapoma, J., Dey, P., Wong-Deyrup, S. W., Dey, B. K. & Halvorsen, K. Exceptional nuclease resistance of paranemic crossover (PX) DNA and crossover-dependent biostability of DNA motifs. *J. Am. Chem. Soc.* **142**, 6814–6821 (2020).
70. Suck, D. DNA recognition by DNase I. *J. Mol. Recognit.* **7**, 65–70 (1994).
71. Jollès, B., Laigle, A., Priebe, W. & Garnier-Suillerot, A. Comparison of DNA sequence selectivity of anthracycline antibiotics and their 3'-hydroxylated analogs. *Chem. Biol.* **100**, 165–176 (1996).
72. Cherepanova, A., Tamkovich, S., Pyshnyi, D., Kharkova, M., Vlassov, V. & Laktionov, P. Immunochemical assay for deoxyribonuclease activity in body fluids. *J. Immunol. Methods* **31**, 96–103 (2007).
73. Douglas, S. M., Marblestone, A. H., Teerapittayanon, S., Vazquez, A., Church, G. M. & Shih, W. M. Rapid prototyping of 3D DNA-origami shapes with caDNAno. *Nucleic Acids Res.* **37**, 5001–5006 (2009).
74. Kim, D.-N., Kilchherr, F., Dietz, H. & Bathe, M. Quantitative prediction of 3D solution shape and flexibility of nucleic acid nanostructures. *Nucleic Acids Res.* **40**, 2862–2868 (2012).
75. Stahl, E., Martin, T. G, Praetorius, F. & Dietz, H. Facile and scalable preparation of pure and dense DNA origami solutions. *Angew. Chem. Int. Ed.* **53**, 12735–12740 (2014).
76. Hung, A. M., Micheel, C. M., Bozano, L. D., Osterbur, L. W., Wallraff, G. M. & Cha, J. N. Large-area spatially ordered arrays of gold nanoparticles directed by lithographically confined DNA origami. *Nat. Nanotechnol.* **5**, 121–126 (2010).
77. Thordarson, P. Determining association constants from titration experiments in supramolecular chemistry. *Chem. Soc. Rev.* **40**, 1305–1323 (2011).